


 Cite this: *Chem. Commun.*, 2023, 59, 12875

 Received 9th September 2023,  
Accepted 4th October 2023

DOI: 10.1039/d3cc04474b

rsc.li/chemcomm

## Controllable fabrication of iron–nickel alloy embedded in nitrogen-doped carbon for oxygen evolution†

 Rong Lin,‡ Lujiao Mao,‡ Yi Ding and Jinjie Qian \*

**Nickel-based electrocatalysts for the oxygen evolution reaction (OER) show the disadvantages of low activity and poor stability. In this paper, an FeNi alloy is wrapped by an amino-modified MOF-5-derived N-doped carbon layer to address these problems. Additionally, the improvement resulting from Fe doping of NiOOH catalysts is theoretically supported.**

The use of transitional fossil fuels is leading to increasingly serious environmental pollution. Therefore, the issue of alternative energy sources needs urgent attention. In this context, hydrogen energy has been developed as a green energy source with high energy density.<sup>1,2</sup> Electrolysis of water provides a convenient method for producing pure hydrogen. However, the slow kinetics of the anodic oxygen evolution reaction (OER) limit the overall water splitting process.<sup>3–5</sup> Commercial noble metal oxides such as IrO<sub>2</sub> and RuO<sub>2</sub> are considered superior OER catalysts, but their high cost, scarcity, and low conductivity have hindered their wide application.<sup>6</sup> Therefore, it is of great significance to explore cost-effective, abundant, and efficient OER catalysts.

Nickel, as a transition metal with good catalytic ability for water oxidation, has been widely reported in the study of OER catalysts. Meng *et al.* developed Ni-based coordination polymer arrays on nickel foam with an overpotential of 350 mV at 20 mA cm<sup>-2</sup>.<sup>7</sup> Rodrigues *et al.* prepared Ni/ZIF-8 composites using calcination and solvothermal treatment with an overpotential of 340 mV at 10 mA cm<sup>-2</sup> and demonstrating good electrocatalytic efficiency.<sup>8</sup> However, the catalytic performance of OER catalysts prepared solely through nickel doping is somewhat insufficient compared to RuO<sub>2</sub>. The synergistic effect of combining two or more transition metals can significantly promote the electron transfer, reduce the reaction barrier of

OER, and improve the catalytic efficiency.<sup>9–13</sup> Meanwhile, the OER stability of Ni doping alone is not satisfactory. However, the cladding effect of nitrogen-doped carbon has been proved to be effective in preventing catalyst corrosion during catalysis and exhibited good stability.<sup>14,15</sup>

On the other hand, metal–organic frameworks (MOFs) are constructed by strong coordination bonds between metal units and organic ligands.<sup>16,17</sup> With their high specific surface area, abundant pore structure, and structural diversity, Ni-based MOF materials have received increasing attention in OER catalysis.<sup>18–20</sup> Due to these structural features, microporous Ni-MOFs show great potential as precursors to prepare MOF-derived carbon nanomaterials with excellent OER catalytic properties.<sup>21,22</sup>

In this study, we successfully obtained FeNi bimetallic compounds embedded into nitrogen-doped carbon (FeNi@NC) from an amino-modified MOF-5 analogue (MOF-5-NH<sub>2</sub>). This effectively improves the activity and stability of single nickel as an OER electrocatalyst. As expected, the prepared FeNi@NC exhibited a smaller overpotential (306 mV) exceeding that of RuO<sub>2</sub> at a current density of 10 mA cm<sup>-2</sup> and demonstrated good stability under an alkaline environment. Finally, we further explored the reasons why bimetallic FeNi exhibited better performance in OER catalysis compared to single Ni using some theoretical calculations.

First, the MOF-5-NH<sub>2</sub> has been successfully fabricated with abundant active sites for adsorbing transition metal. Generally, microporous MOF-5 is endowed with rigid Zn<sub>4</sub>O-based building units, which are structurally bridged by terephthalic acid (H<sub>2</sub>BDC) to form an open but robust structure.<sup>23</sup> While MOF-5-NH<sub>2</sub> essentially exhibits the same topological features as MOF-5, it carries an amino group within each H<sub>2</sub>BDC (Fig. S1, ESI†).<sup>24</sup> In this case, the tetragonal channels of ~13.06 Å along the *a*-axis are functionalized with amino groups to effectively capture Fe(III) and Ni(II) ions (Fig. 1b and Fig. S2, ESI†).<sup>25</sup> The PXRD spectra of the as-obtained and desolvated samples were in good agreement with the simulated MOF-5 (Fig. 1c). Three prominent diffraction peaks at 6.8°, 9.8° and

Key Laboratory of Carbon Materials of Zhejiang Province, College of Chemistry and Materials Engineering, Wenzhou University, Wenzhou 325035, Zhejiang, P. R. China. E-mail: jinjieqian@wzu.edu.cn

† Electronic supplementary information (ESI) available. See DOI: <https://doi.org/10.1039/d3cc04474b>

‡ These authors contributed equally to this work.

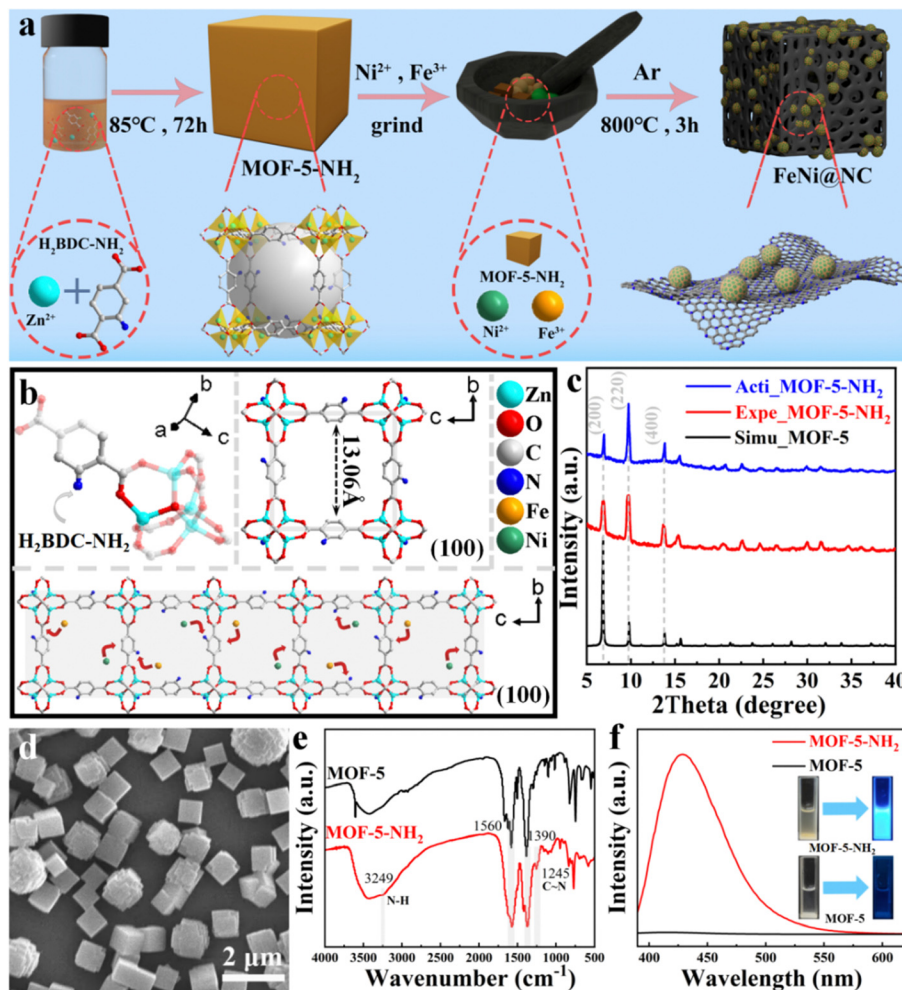


Fig. 1 (a) Stepwise preparation of FeNi@NC nanomaterial. (b) Asymmetric unit, pore size, and amino groups coordinated with inserted iron and nickel ions within MOF-5-NH<sub>2</sub>. (c) PXRD patterns. (d) SEM image of MOF-5-NH<sub>2</sub>. (e) FTIR spectra. (f) Fluorescence emission spectra of various MOFs.

13.8° corresponded to the (200), (220), and (400) planes, respectively. This suggested that the obtained MOF-5-NH<sub>2</sub> possessed high purity and crystallinity, displaying nanocubes with an average length of 0.85 μm in Fig. 1d and Fig. S4 (ESI†). When compared with unmodified MOFs, MOF-5-NH<sub>2</sub> exhibited a characteristic peak at 3249 cm<sup>-1</sup> corresponding to N-H stretching (Fig. 1e), while the one at 1245 cm<sup>-1</sup> was associated with the C-N stretching.<sup>26,27</sup> In Fig. 1f, the fluorescence emission spectra revealed a strong emission signal at 427 nm for MOF-5-NH<sub>2</sub>, whereas MOF-5 showed minimal emission to further verify the effective amino functionalization.<sup>25</sup> Lastly, its N<sub>2</sub> isotherms presented a type I one, with its pore size primarily distributed in the range of 0.5–2 nm with abundant micropores (Fig. S3, ESI†).

After pyrolysis, the irregular particles with diameters of 35–55 nm were dispersed into porous N-doped carbon layers in Fig. 2a, b and Fig. S5, S6 (ESI†). This even distribution of nanosized FeNi alloys might be ascribed to the N-doping to effectively prevent the agglomeration.<sup>28,29</sup> There were two types of lattice fringes of 3.362 and 2.076 Å corresponding to the graphitic carbon (002) plane and FeNi<sub>3</sub> (111) plane, respectively

(Fig. 2c and Fig. S7, ESI†). Fig. 2d shows three distinct diffraction peaks at 44.3°, 51.5°, 76.6° attributed to the (111), (200), and (220) planes of FeNi<sub>3</sub> (PDF#38-0419), respectively. The N<sub>2</sub> curves of FeNi@NC belonged to the type I isotherm that constituted a large BET surface area of 452.39 m<sup>2</sup> g<sup>-1</sup> (Fig. S9 and Table S2, ESI†). As shown in Fig. 2e, XPS was further utilized to reveal the chemical state where the full survey spectrum confirms the coexistence of Fe, Ni, C, N and O for FeNi@NC. There were four subpeaks at 398.1, 399.1, 400.0, 402.1 eV attributed to pyridinic-N, pyrrolic-N, graphitic-N and oxidized-N, respectively (Fig. 2f). The high content of graphite/pyridine nitrogen would be beneficial to the mass transfer of oxygen intermediates during OER.<sup>30</sup> Fig. 2g revealed six subpeaks as 709.0 eV (Fe 2p<sub>3/2</sub>) and 722.6 eV (Fe 2p<sub>1/2</sub>) for Fe(0), 711.3 eV (Fe 2p<sub>3/2</sub>) and 724.6 eV (Fe 2p<sub>1/2</sub>) for Fe(II), and 714.0 eV (Fe 2p<sub>3/2</sub>) and 727.2 eV (Fe 2p<sub>1/2</sub>) for Fe(III). Finally, the presence of metallic Ni(0) was observed at 854.9 and 872.9 eV, and the Ni(II) 2p<sub>3/2</sub> and 2p<sub>1/2</sub> at 856.1 and 874.0 eV, along with a pair of satellite peaks (862.1 and 879.6 eV, Fig. 2h). The detailed XPS data for the control sample of FeNi@C is shown in Fig. S11 (ESI†). These results demonstrated that the cladding effect of

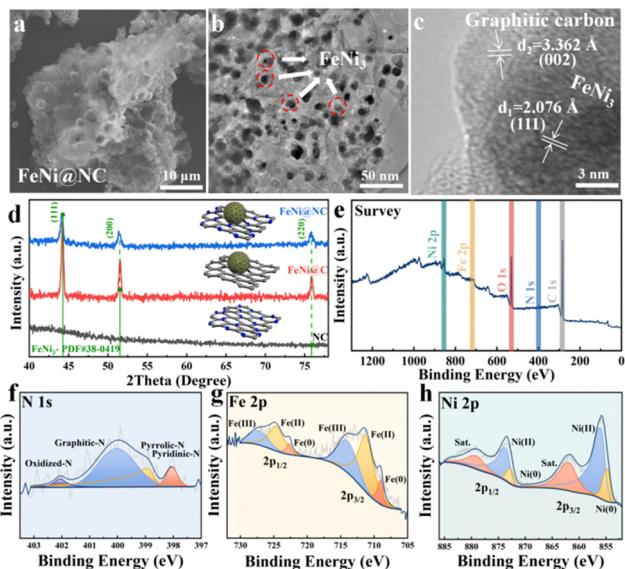


Fig. 2 (a)–(c) SEM, TEM and HR-TEM images of FeNi@NC. (d) PXRD patterns of various MOF-derived carbon nanomaterials. (e) The full XPS survey spectrum of FeNi@NC. The deconvoluted XPS spectra of (f) N 1s, (g) Fe 2p, (h) Ni 2p.

N-doped carbon was favourable for anchoring and dispersing FeNi<sub>3</sub> particles, exposing more active species for efficient OER.

A three-electrode system was utilized to investigate the electrocatalytic OER performance, and commercial RuO<sub>2</sub> was used for comparison. Firstly, FeNi@NC exhibited the lowest overpotential ( $\eta_{10}$ ) of 306 mV at 10 mA cm<sup>-2</sup>, much lower than FeNi@C (334 mV), NC (454 mV) and RuO<sub>2</sub> (331 mV) in Fig. 3a and Table S4 (ESI<sup>†</sup>). The smallest Tafel slope value was also observed for FeNi@NC (97.56 mV dec<sup>-1</sup>), indicating faster reaction kinetics than the other samples (Fig. 3b). Subsequently, the double layer capacitance ( $C_{dl}$ ) values in the non-Faraday region of FeNi@NC, FeNi@C, NC and RuO<sub>2</sub> were calculated to be 14.36, 4.94, 2.17 and 4.72 mF cm<sup>-2</sup>, respectively, indicative of a superior electrochemical active area for enhanced catalytic activity of FeNi@NC (Fig. 3c and Fig. S12, ESI<sup>†</sup>). The electrochemical impedance spectroscopy (EIS) analysis in Fig. 3d showed that FeNi@NC had an impedance of 91.2  $\Omega$ , which was much smaller than that of FeNi@C (714.1  $\Omega$ ), NC (1370.2  $\Omega$ ) and RuO<sub>2</sub> (183.8  $\Omega$ ). Using a rotating ring-disk electrode (RRDE) with negligible ring current ( $I_{ring}$ ) compared to the ring-disk current ( $I_{disk}$ ), the calculated average number of electron transfers ( $N$ ) revealed a quasi-4-electron process (Fig. S13, ESI<sup>†</sup>). In Fig. S14 (ESI<sup>†</sup>), the potential of the ring electrode was 0.4 V, and the collected  $I_{ring}$  was  $\sim$ 39.85 mA, while the  $I_{disk}$  was kept at 200  $\mu$ A, providing a high Faraday efficiency (FE) of nearly 100%. To evaluate the durability of FeNi@NC, a 10 hour potential detection at a constant voltage of 1.64 V and a linear sweep voltammetry (LSV) test were performed, which showed an overpotential decrease of only 13 mV, and a satisfactory current retention of 88.03% (Fig. 3e and f). In conclusion, the synthesized FeNi@NC catalyst exhibited competitive OER behaviour compared to previously reported electrocatalysts (Table S5, ESI<sup>†</sup>).

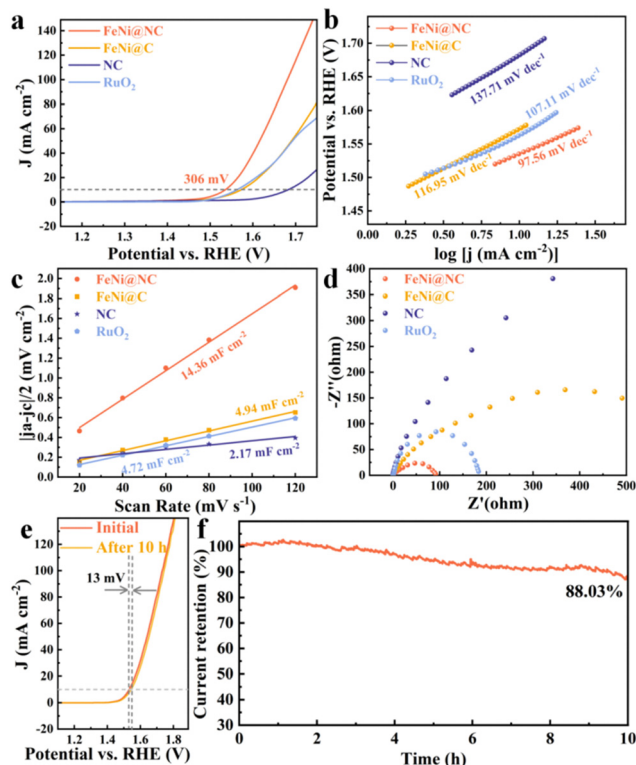


Fig. 3 (a) LSV curves, (b) Tafel slopes, (c)  $C_{dl}$  profiles and (d) EIS curves of the prepared OER catalysts. (e) LSV curves before/after 10 hours. (f) The  $i-t$  stability test.

The enhanced electrocatalytic OER property was further demonstrated by theoretical DFT calculations. In this case, the stepwise reaction processes of NiOOH and Ni(Fe)OOH as active sites were mechanistically modeled for FeNi@NC and FeNi@C, as reported in previous studies, respectively.<sup>30–33</sup> Details of the reconstruction of FeNi species to Ni(Fe)OOH are shown in Fig. S15 and S16 (ESI<sup>†</sup>). Generally speaking, the formation of \*O radicals is regarded as a potentially decisive step in OER. Compared to pure NiOOH (State IV,  $\Delta G_{3 \rightarrow 4} = 2.06$  eV), Fe-doped Ni(Fe)OOH contained a high-spin 3d<sup>4</sup> Fe(IV) site, which stably generated the unpaired electrons in \*O thereby significantly reducing the required energy (1.68 eV, Fig. 4 and Fig. S17, S18, ESI<sup>†</sup>). Moreover, the N-doping in the carbon layer further contributed to the conductivity of FeNi@NC, facilitating the overall OER procedure in comparison with

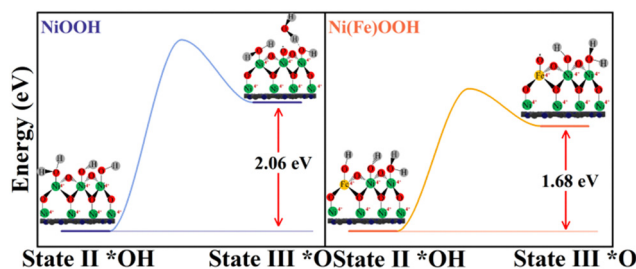


Fig. 4 Free Gibbs energies involved in the rate determining step for pure NiOOH (left) and Fe-doped NiOOH (right).

FeNi@C.<sup>34–37</sup> For more details on the calculated free energies for NiOOH and Ni(Fe)OOH, please refer to Fig. S19 in the ESI.†

In summary, herein we present one type of MOF-derived porous FeNi@NC electrocatalyst with satisfactory electrochemical efficiency and stability. This catalyst can provide a current density of 10 mA cm<sup>-2</sup> at a small overpotential of 306 mV with moderate stability under a basic solution. Meanwhile, DFT calculations show that the doping of Fe effectively compensates for the insufficient electrochemical efficiency of the nickel-based catalyst. This method can be effectively extended to other MOF-derived porous carbon nanomaterials for energy conversion and storage.

Rong Lin and Lujiao Mao: methodology, data curation, formal analysis, investigation, validation, writing – original draft. Yi Ding: data curation, formal analysis, writing – original draft. Jinjie Qian: conceptualization, formal analysis, funding acquisition, investigation, project administration, supervision, writing – review & editing.

This work was financially supported by National Natural Science Foundation of China (21601137), Natural Science Foundation of Zhejiang Province (LQ16B010003), Basic Science and Technology Research Project of Wenzhou, Zhejiang Province (H20220001).

## Conflicts of interest

There are no conflicts to declare.

## Notes and references

- Z. P. Izkovits, J. M. Evans, M. C. Meier, K. M. Papadantonakis and N. S. Lewis, *Energy Environ. Sci.*, 2021, **14**, 4740–4759.
- S. Chu and A. Majumdar, *Nature*, 2012, **488**, 294–303.
- G. Zhou, P. Wang, H. Li, B. Hu, Y. Sun, R. Huang and L. Liu, *Nat. Commun.*, 2021, **12**, 4827.
- Y. Wang, S. Tao, H. Lin, G. Wang, K. Zhao, R. Cai, K. Tao, C. Zhang, M. Sun, J. Hu, B. Huang and S. Yang, *Nano Energy*, 2021, **81**, 105606.
- J. Du, F. Li and L. Sun, *Chem. Soc. Rev.*, 2021, **50**, 2663.
- C. C. L. McCrory, S. Jung, J. C. Peters and T. F. Jaramillo, *J. Am. Chem. Soc.*, 2013, **135**, 16977–16987.
- C. Meng, Y. Cao, Y. Luo, F. Zhang, Q. Kong, A. A. Alshehri, K. A. Alzahrani, T. Li, Q. Liu and X. Sun, *Inorg. Chem. Front.*, 2021, **8**, 3007–3011.
- C. D. Rodrigues, L. S. Bezerra, E. S. F. Cardoso, G. V. Fortunato, P. K. Boruah, M. R. Das, M. R. V. Lanza and G. Maia, *Electrochim. Acta*, 2022, **435**, 141362.
- P. Kamakoti, *J. Membr. Sci.*, 2003, **225**, 145–154.
- Y. Guo, Q. Huang, J. Ding, L. Zhong, T. Li, J. Pan, Y. Hu, J. Qian and S. Huang, *Int. J. Hydrogen Energy*, 2021, **46**, 22268–22276.
- X. Li, H. Zhang, Q. Hu, W. Zhou, J. Shao, X. Jiang, C. Feng, H. Yang and C. He, *Angew. Chem., Int. Ed.*, 2023, **62**, e202300478.
- Z. Pei, H. Zhang, Z.-P. Wu, X. F. Lu, D. Luan and X. W. Lou, *Sci. Adv.*, 2023, **9**, eadh1320.
- S. Kang, C. Im, I. Spanos, K. Ham, A. Lim, T. Jacob, R. Schlögl and J. Lee, *Angew. Chem., Int. Ed.*, 2022, **61**, e202214541.
- P. Jiang, J. Chen, C. Wang, K. Yang, S. Gong, S. Liu, Z. Lin, M. Li, G. Xia, Y. Yang, J. Su and Q. Chen, *Adv. Mater.*, 2018, **30**, 1705324.
- L.-F. Gu, J.-J. Chen, T. Zhou, X.-F. Lu and G.-R. Li, *Nanoscale*, 2020, **12**, 11201.
- H. Furukawa, K. E. Cordova, M. O’Keeffe and O. M. Yaghi, *Science*, 2013, **341**, 1230444.
- Q. Ren, J.-Q. Wu, J.-W. Zhao, C.-F. Li, L. Gong, D.-D. Zhou and G.-R. Li, *Chem. Commun.*, 2020, **56**, 7722–7725.
- C. Guo, Y. Jiao, Y. Zheng, J. Luo, K. Davey and S.-Z. Qiao, *Chem*, 2019, **5**, 2429–2441.
- S. Xu, Q. Huang, J. Xue, Y. Yang, L. Mao, S. Huang and J. Qian, *Inorg. Chem.*, 2022, **61**, 8909–8919.
- X. Sun, S. Wang, Y. Hou, X. Lu, J. Zhang and X. Wang, *J. Mater. Chem. A*, 2023, **11**, 13089.
- A. Mahmood, W. Guo, H. Tabassum and R. Zou, *Adv. Energy Mater.*, 2016, **6**, 1600423.
- V. Maruthapandian, S. Kumaraguru, S. Mohan, V. Saraswathy and S. Muralidharan, *ChemElectroChem*, 2018, **5**, 2795–2807.
- H. Li, M. Eddaoudi, M. O’Keeffe and O. M. Yaghi, *Nature*, 1999, **402**, 276–279.
- Y. Yang, Q. Huang, Q. Sun, J. Xue, S. Xu, L. Mao, X. Zhou, D. Yu, Q. Li and J. Qian, *ACS Sustainable Chem. Eng.*, 2022, **10**, 8641–8649.
- S.-W. Lv, J.-M. Liu, C.-Y. Li, N. Zhao, Z.-H. Wang and S. Wang, *Chem. Eng. J.*, 2019, **375**, 122111.
- X. An, Q. Tan, S. Pan, H. Liu and X. Hu, *Spectrochim. Acta, Part A*, 2021, **247**, 119073.
- J. F. Kurisingal, Y. Rachuri, Y. Gu, Y. Choe and D.-W. Park, *Chem. Eng. J.*, 2020, **386**, 121700.
- Y. Yu, Z. Peng, M. Asif, H. Wang, W. Wang, Z. Wu, Z. Wang, X. Qiu, H. Tan and H. Liu, *ACS Sustainable Chem. Eng.*, 2018, **6**, 11587–11594.
- G. Fu, Z. Cui, Y. Chen, Y. Li, Y. Tang and J. B. Goodenough, *Adv. Energy Mater.*, 2017, **7**, 1601172.
- D. Chen, Q. Sun, C. Han, Y. Guo, Q. Huang, W. A. Goddard and J. Qian, *J. Mater. Chem. A*, 2022, **10**, 16007–16015.
- H. Shin, H. Xiao and W. A. Goddard, *J. Am. Chem. Soc.*, 2018, **140**, 6745–6748.
- H. Lei, L. Ma, Q. Wan, S. Tan, B. Yang, Z. Wang, W. Mai and H. J. Fan, *Adv. Energy Mater.*, 2022, **12**, 2202522.
- B. Zhang, Z. Wu, W. Shao, Y. Gao, W. Wang, T. Ma, L. Ma, S. Li, C. Cheng and C. Zhao, *Angew. Chem., Int. Ed.*, 2022, **61**, e202115331.
- X. Wang, H. Huang, J. Qian, Y. Li and K. Shen, *Appl. Catal., B*, 2023, **325**, 122295.
- X. Wang, A. Dong, Y. Hu, J. Qian and S. Huang, *Chem. Commun.*, 2020, **56**, 10809.
- Y. Jin, W. Huo, X. Zhou, L. Zhang, Y. Li, S. Yang, J. Qian, D. Cai, Y. Ge, Z. Yang and H. Nie, *Chem. Commun.*, 2023, **59**, 183.
- W. Huo, X. Zhou, Y. Jin, C. Xie, S. Yang, J. Qian, D. Cai, Y. Ge, Y. Qu, H. Nie and Z. Yang, *Small*, 2023, **19**, 2207847.